Contents lists available at ScienceDirect

Transactions of Nonferrous Metals Society of China

36(2026) 694−708

www.tnmsc.cn

Effect of texture and grain structure on tensile strength and anisotropy in annealed Al−Cu−Mg alloy with high Cu/Mg mass ratio

Guang-yu HE [a,b], Zhi-yi LIU [a,b,*], Yang-cheng HU [a,b], Qian JIANG [a,b], M. S. QURASHI [a,b]

[a] School of Materials Science and Engineering, Central South University, Changsha 410083, China;

[b] Key Laboratory of Nonferrous Metal Materials Science and Engineering, Ministry of Education, Central South University, Changsha 410083, China

Abstract: Texture and grain structure evolution during annealing and their effects on tensile strength and anisotropy were studied using XRD, DSC, SEM, EBSD and TEM. The results indicate that elevated rolling temperatures reduce the $f(g)_{\text{max(Copper)}}/f(g)_{\text{max(Brass)}}$ ratio, increase S−Brass fine bands, and promote S-dispersoid precipitation, leading to finer recrystallized grains. Dominant recrystallization textures transform from Goss + P to Goss and then to Goss + Cube with increasing rolling temperature. Annealing at 350 °C shows four tensile strength response stages: fast softening I, rapid strengthening II, slow strengthening III, and slow softening IV. The transition from Stages I to II is driven by the formation of strong Goss and P textures, and Stage IV is linked to enhanced Cube texture. Plates with Goss + Cube textures and fine equiaxed grains exhibit the lowest YS/UTS ratio and minimal anisotropy.

Keywords: Al−Cu−Mg alloy; Goss texture; P texture; Cube texture; grain structure; tensile strength; anisotropy

1 Introduction

Aged Al−Cu−Mg-based alloys, crucial for aerospace applications, are valued for their light weight, high strength, superior damage tolerance, and better fatigue resistance [1−3]. Their improved yield stress primarily results from grain refinement, precipitation/cluster strengthening, and solid solution strengthening [4−8]. Nanocrystalline grains can enhance tensile strength to ~1 GPa in 2024 alloy but require complex preparation conditions, limiting their application [4]. Mechanical properties are further influenced by grain morphology and crystallographic orientation [9−12].

Annealing treatments, including temperature and heating rate, significantly affect softening behavior and anisotropy [9,13,14]. Plates with β-fiber or mixed Cube plus rolling textures exhibit greater strength, lower ductility, and pronounced anisotropy compared to soft-annealed plates dominated by Cube texture [9]. Texture is main factor influencing the occurrence of anisotropy for Al alloy plate, with anisotropy reduction critical for engineering needs. In Al−Mn alloys, higher heating rates produce finer grains, fewer elongated grains, dominant Cube texture, and reduced flow stress [13]. The reduced flow stress is related to less precipitation which overweights the minor grain size effect. Crystallographic textures like Goss enhance yield strength in naturally aged Al−Cu−Mg alloy via the improved Taylor factors; while texture with a combination of ⟨100⟩ and ⟨110⟩ promotes both multiple slip and twinning and enhances hardening in stainless steel 316 L [10,15]. On the other hand, the crystallographic orientations or textures (such as Goss and P) also play an important role in enhancing fatigue resistance [16−18]. In Al−Cu−Mg alloys,

---

Corresponding author: *Zhi-yi LIU, Tel: +86-731-88836927, E-mail: liuzhiyi@csu.edu.cn

https://doi.org/10.1016/S1003-6326(25)66991-3

Received 3 July 2024; accepted 7 January 2025

Goss and P grains can facilitate crack deflection when they possess large twist or tilt angles with neighboring grains [18−20]. Furthermore, the {111} planes of these grains are close to maximum critical resolved shear stress (CRSS) direction, raising the energy required for crack propagation. Thus, recrystallized Goss and P texture components are desired in final microstructure. Controlling texture and grain structure is essential for improving mechanical properties of Al alloys.

Recrystallization textures typically arise from specialized deformation textures via the migration of coincidence site lattice (CSL) boundaries, such as Goss from Brass by CSL $\sum 9$ [21], and Cube from S by CSL $\sum 7$ [22]. P component is uncommon in 2000 series alloys but common in Al−Mn alloys [23−25]. P texture depends on the sequence of recrystallization and precipitation, and its abnormal growth process is related to deformation Copper texture [25]. Deformation texture is affected by microchemistry, stacking fault energy (SFE), and thermomechanical processing such as rolling temperature and reduction [26−30]. Rolling temperature can modify dislocation slip manner and dynamic recrystallization level, thus leads to different deformation texture and microstructure. However, its effects on recrystallization textures (Goss, P, and Cube), grain structure, and final mechanical properties in 2000 series alloys have not been reported in detail. In the present work, we investigated the impact of rolling temperature on recrystallization texture and grain structure, and examined the mechanical property evolution of an Al−Cu−Mg alloy with a high Cu/Mg mass ratio during annealing. Furthermore, the relationships between texture, grain structure and anisotropy behavior were established.

2 Experimental

2.1 Materials and treatments

The chemical composition of the studied Al−Cu−Mg alloy was 4.3% Cu, 1.0% Mg, 0.53% Mn, 0.08% Ti, <0.035% Fe, <0.025% Si, and balance aluminum (in wt.%). Ingots were initially homogenized at (465 °C, 48 h) + (475 °C, 72 h), and then hot rolled to 2 mm-thick plates at blooming temperatures of 390, 420, and 450 °C, designated as RT-39, RT-42, and RT-45 alloys. Differential scanning calorimetry (DSC) was conducted on a Netzsch STA449C instrument at various heating rates up to 500 °C to estimate the recrystallization temperature range. RT-39 samples were annealed at 310−370 °C in 20 °C intervals for 4 h to optimize annealing temperature (350 °C for 4 h) for the development of strong Goss, P and Cube textures. All alloys were annealed at 350 °C for 5 min to 8 h to investigate the relationship between tensile properties and annealing time. Samples for in-plane anisotropy were annealed at 350 °C for 4 h.

2.2 Texture and microstructure characterization

Samples for XRD and EBSD were electropolished in a solution of 8% perchloric acid and 92% ethanol at 22−24 V for 30−50 s. A Bruker D8 Discover X-ray diffractometer (XRD) system was utilized to measure (111), (200), and (220) pole figures using the Schulz back-reflection method. Orientation distribution functions (ODFs) were calculated via the series expansion method ($L_{\max}=16$) [31]. ODFs are presented as φ_2 section plots with isointensity contours in the Euler space defined by Euler angles φ_1, Φ, and φ_2. Macrotexture volume fractions were calculated via the method per Ref. [32]. Electron back-scattered diffraction (EBSD) on a Sirion 200 field emission gun scanning electron microscope (SEM) characterized microtextures and micro-structures, with analysis via both ATEX [33] and AZTEC software. Second-phase particles were characterized in backscattered electron (BSE) mode on a Quanta 200 SEM at 25 kV, and analyzed with Image-Pro Plus 6.0 software. Transmission electron microscopy (TEM) samples were prepared by twin-jet electropolishing in a solution of 70% ethanol and 30% nitric acid at –25 °C and were observed on a Tecnai G^2 20 ST microscope operating at 200 kV.

2.3 Mechanical property tests

Tensile tests were performed under 2 mm/min at room temperature per standard ISO 6892−1:2009. Figure 1(a) shows sample sizes for tensile tests, while Fig. 1(b) illustrates tensile tests under in-plane angles (α) of 0°, 22.5°, 45°, and 90° to the TD to assess anisotropy, where α denotes the in-plane angle between the center axis of tensile sample and transverse direction (TD), and ND and RD represent normal and rolling directions. Microhardness profiles were measured at a load of 5 kg for 15 s, averaging five points.

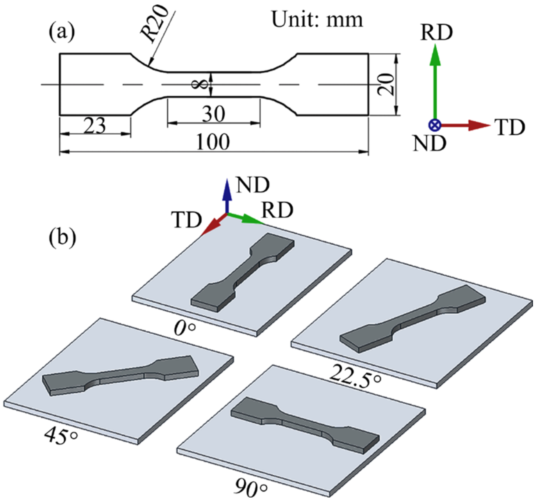

Fig. 1 (a) Size of sample used for tensile tests; (b) Schematic diagram showing tensile tests under different in-plane angles (α) of 0°, 22.5°, 45°, and 90° to TD, to determine anisotropy

3 Results

3.1 XRD characterization and DSC curves

In the RT-39 alloy, rolling texture components consist of strong Copper {112}⟨111⟩, S {123}⟨634⟩, and Brass {011}⟨211⟩ with maximum intensities $f(g)_{\max}$ of 8.7, 5.79 and 8.7, respectively, and a ratio of $f(g)_{\max(\text{Copper})}/f(g)_{\max(\text{Brass})}=1$ (Fig. 2(a)). As the rolling temperature increases from 390 to 450 °C, the $f(g)_{\max(\text{Copper})}/f(g)_{\max(\text{Brass})}$ ratio decreases from 1 to 0.49 (Figs. 2(a−c)). The RT-45 alloy is dominated by the sharp Brass texture with an intensity of 10.81. The volume fractions of Copper, S, and Goss {011}⟨100⟩ components decrease with higher rolling temperatures (Table 1).

Figure 3 shows that wide exothermic peaks appear in all rolled samples at a heating rate of 10 °C/min, narrowing slightly with increasing rolling temperature. These peaks, associated with recrystallization processes [34,35], occur between 250 and 300 °C. At a heating rate of 40 °C/min, the RT-39 alloy displays a noticeable exothermic peak near 350 °C. After annealing RT-39 alloy at 310 and 330 °C for 4 h, rolling components persist (Figs. 4(a, b)), though Copper and S component intensities decline, with orientation lines moving toward the typical Brass position. At 350 °C, RT-39 alloy develops intense Goss and P {011}⟨122⟩ textures, with maximum intensities of 11.51 and 7.66, respectively (Fig. 4(c)). As the annealing temperature rises to 370 °C, the intensity of P texture decreases (Fig. 4(d)), confirming 350 °C as the

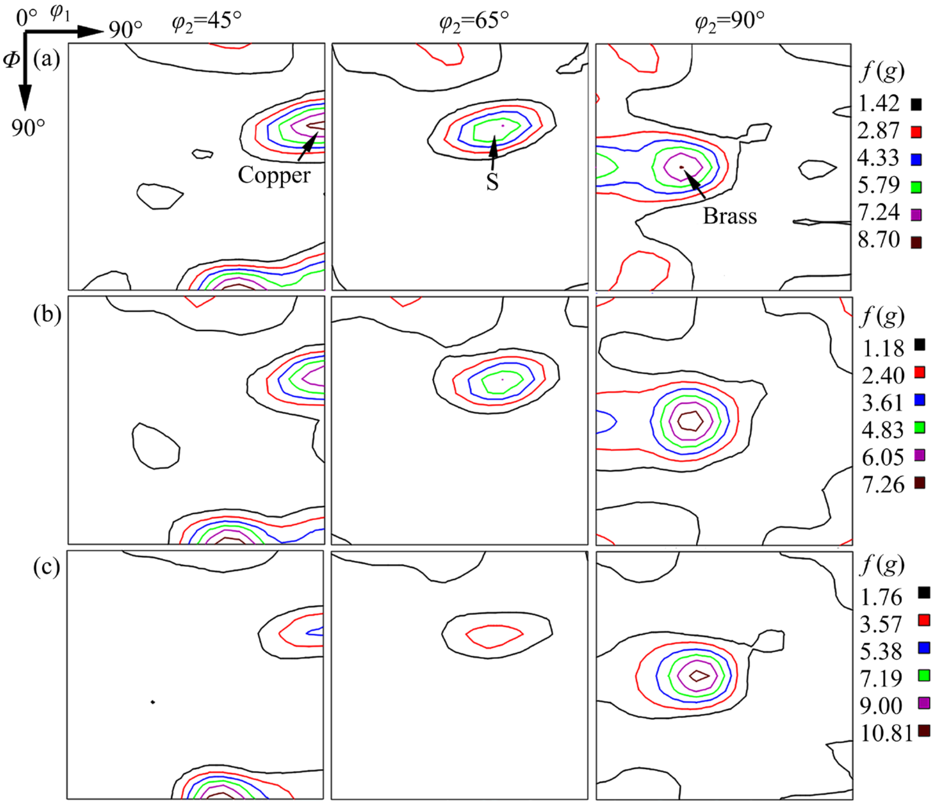

Fig. 2 φ_2=45°, 65° and 90° sections of ODF for three rolled alloys: (a) RT-39 alloy; (b) RT-42 alloy; (c) RT-45 alloy

Table 1 Volume fractions of rolling texture components (%)

Component	RT-39 alloy	RT-42 alloy	RT-45 alloy
Copper	20.85	16.06	10.39
S	17.09	14.73	6.10
Brass	20.97	22.13	29.40
Goss	12.14	7.06	4.85

optimal annealing temperature for the three alloys. Figure 5 illustrates the texture evolution at 350 °C with annealing time. After 4 h, RT-39 alloy shows strong Goss and P + weak Cube {001}⟨100⟩ textures (Fig. 5(a)), RT-42 alloy exhibits strong Goss + weak P and Cube (Fig. 5(b)), and RT-45 alloy presents strong Goss + Cube components (Fig. 5(c)). After 8 h, Cube intensifies while Goss and P weaken, with RT-45 alloy having a predominantly Cube texture (Figs. 5(d−f)). Volume fractions of recrystallization texture are listed in Table 2, with early-stage microstructure changes analyzed via EBSD in Section 3.2.

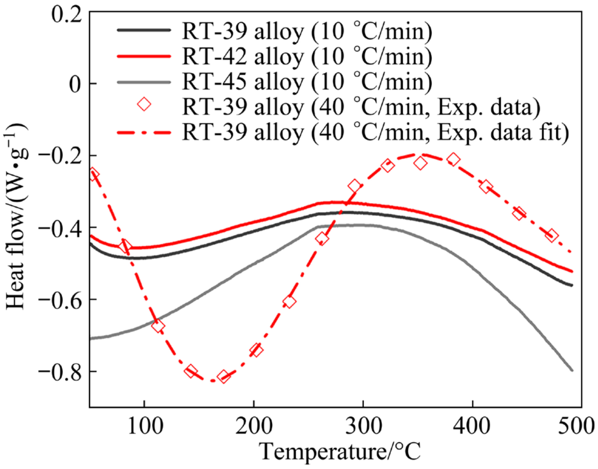

Fig. 3 DSC curves for rolling samples tested at different heating rates up to 500 °C

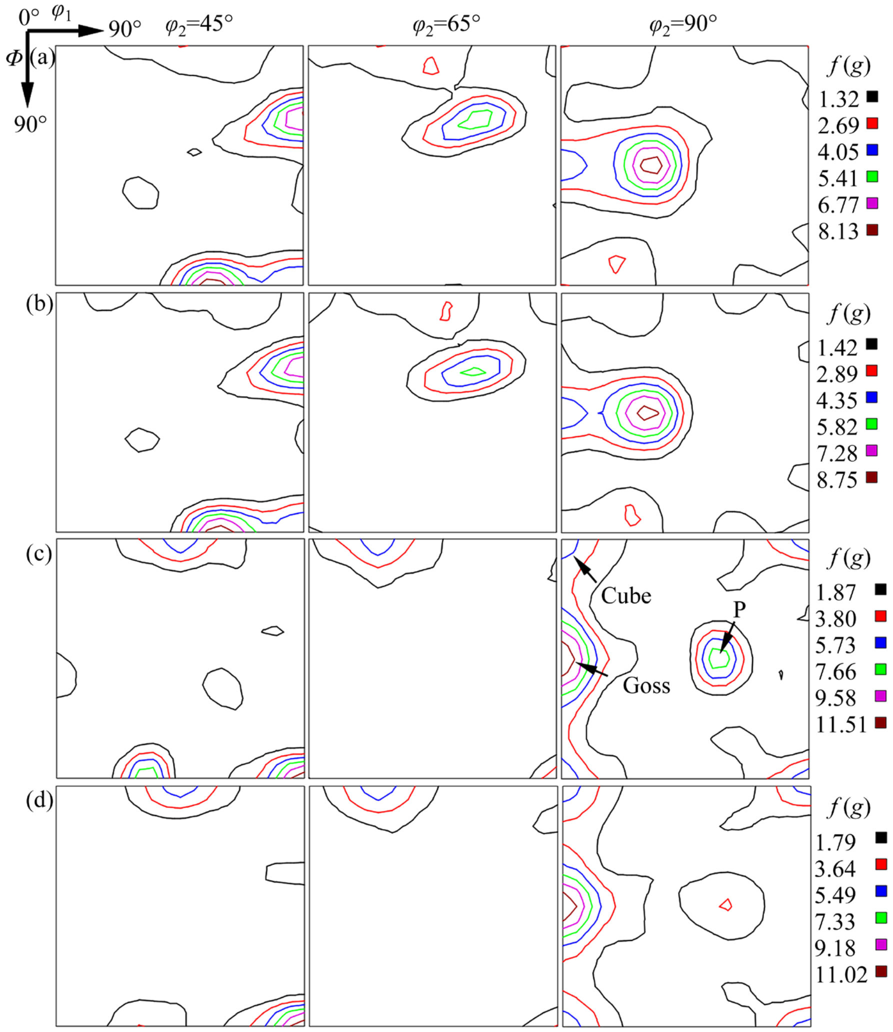

Fig. 4 φ_2=45°, 65° and 90° sections of ODF for RT-39 alloy after annealing at different temperatures for 4 h: (a) 310 °C; (b) 330 °C; (c) 350 °C; (d) 370 °C

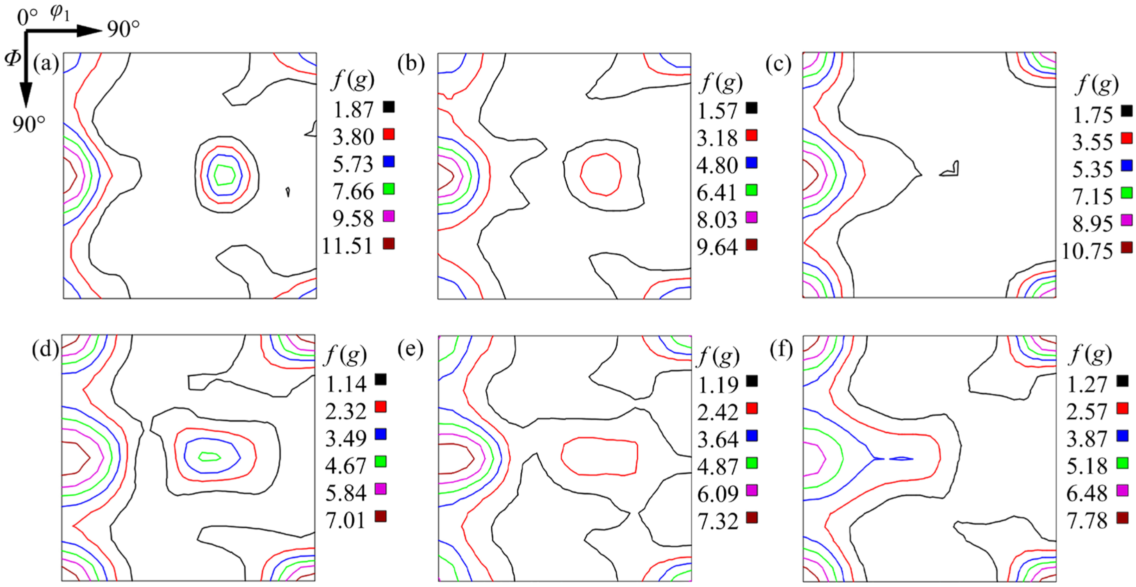

Fig. 5 φ_2=90° sections of ODF for three alloys after annealing at 350 °C for various time: (a−c) 4 h; (d−f) 8 h; (a, d) RT-39 alloy; (b, e) RT-42 alloy; (c, f) RT-45 alloy

Table 2 Volume fractions of annealing texture components (350 °C for 4 h) (%)

Component	RT-39 alloy	RT-42 alloy	RT-45 alloy
Goss	21.54	20.29	29.51
P	14.91	8.96	0
Cube	8.7	10.47	18.04

3.2 SEM, EBSD and TEM results

Figure 6 shows SEM-BSE images of second-phase particles in rolling samples annealed at 350 °C, where white particles are identified as Al_2Cu (θ-particles) and Al_2CuMg (S-dispersoids) [30,36]. θ-particles, large and grain-boundary distributed along the RD direction (Figs. 6(a−c)), differ slightly in content across alloys, while S-dispersoids are small and uniformly dispersed within grains (Figs. 6(d−l)). After annealing for 10 min, the number densities of S-dispersoids are 4.64×10^{11}, 6.21×10^{11}, and 7.17×10^{11} m^{-2} for RT-39, RT-42 and RT-45 alloys, respectively (Figs. 6(d−f)). Elevated rolling temperature leads to increasing the number density of S-dispersoids due to dynamic precipitation. Prolonged annealing to 4 h caused no notable change in S-dispersoid content (Figs. 6(g−l)).

After annealing at 350 °C for 10 min, RT-39 and RT-42 alloys retained strong Copper textures (Figs. 7(a, b), 8(a, b)), while RT-45 alloy developed recrystallized Goss and Cube nuclei exceeding 20 μm (Figs. 7(c, f), and 8(c)). ODF at φ_2= 90° suggests Brass transition into Goss along the α-fiber in RT-45 alloy, and texture evolution from Copper through S to Brass along β-fiber with increasing rolling temperature. Sub-grain/grain sizes for RT-39, RT-42, and RT-45 alloys are 1.99, 2.01, and 3.06 μm, respectively (Figs. 7(d−f)), with more S−Brass fine bands (white arrows) and recrystallized nuclei (white ellipses) at higher rolling temperatures. Figures 7(g−i) show the microstructure of the rolled samples after annealing at 350 °C for 30 min. The RT-39 and RT-42 alloys exhibit coarse, elongated grains along the RD direction, while the RT-45 alloy shows fine, equiaxed grains. The average grain sizes are 323.6, 104.7 and 87.5 μm for RT-39, RT-42, and RT-45 alloys, respectively (Figs. 7(j−l)). Clearly, increasing the rolling temperature results in finer recrystallized grain size. The texture of RT-39 alloy consists of high-intensity Goss + P (Fig. 9(a)), RT-42 alloy has strong Goss + weak P (Fig. 9(b)), and RT-45 alloy is characterized by strong Goss + Cube (Fig. 9(c)). After annealing at 350 °C for 4 h, the grain structures of RT-39 and RT-42 alloys show slight changes, while RT-45 develops typical equiaxed grains (Figs. 7(m−o)). The average grain sizes are 336.5, 116.4, and 68.7 μm, respectively (Figs. 7(p−r)). The microtextures show low Cube content in RT-39 and RT-42 alloys (Figs. 9(d−e)). Prolonged annealing time enhances Goss and Cube textures while weakening P texture in RT-39 and increases Cube texture in RT-42 and RT-45 alloys (see Fig. 5).

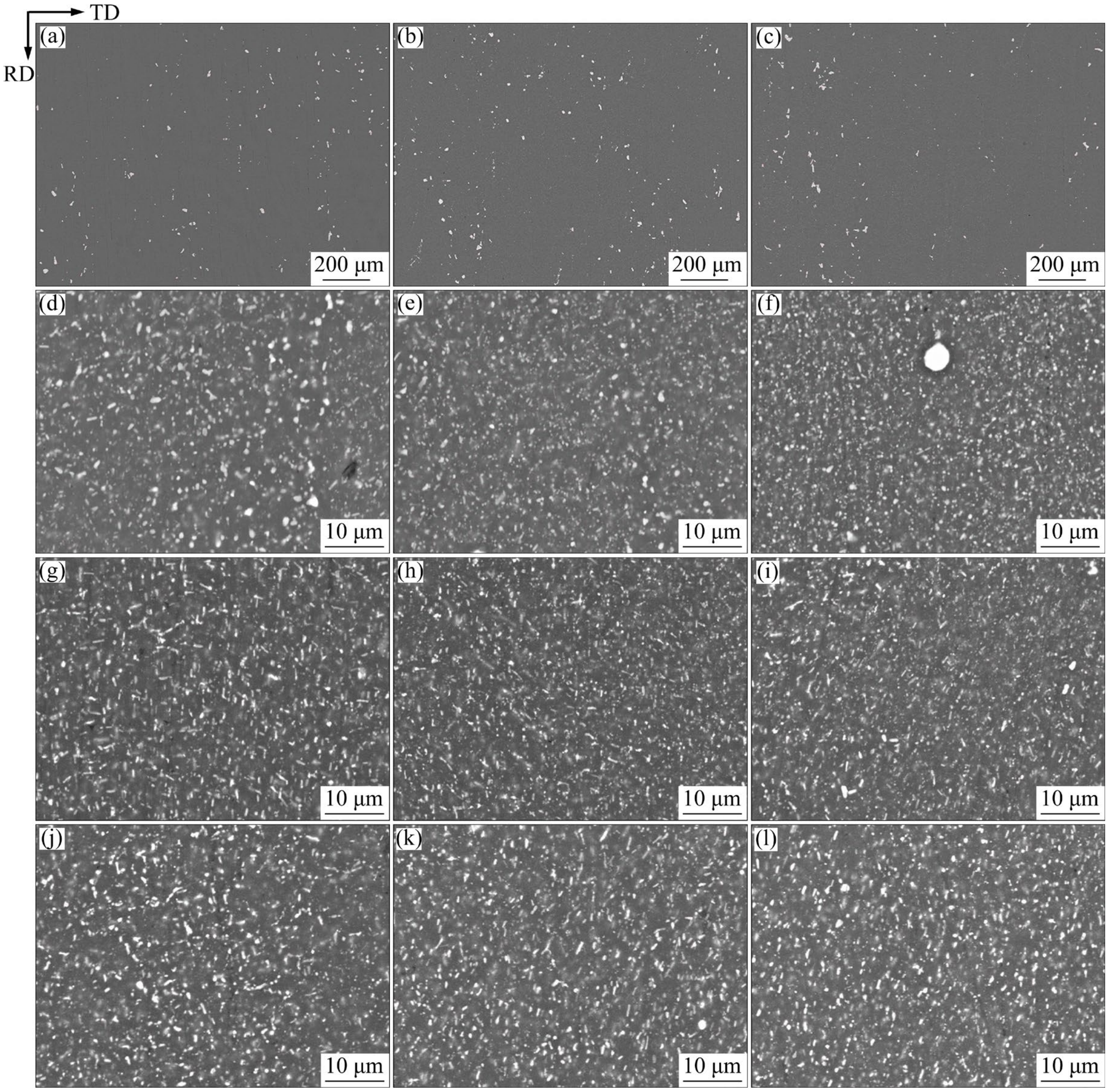

Fig. 6 SEM results showing secondary-phase particles of rolling samples after annealing at 350 °C for various time: (a−c) θ-particles (4 h); (d−l) S-dispersoids; (a, d, g, j) RT-39 alloy; (b, e, h, k) RT-42 alloy; (c, f, i, l) RT-45 alloy; (d−f) 10 min; (g−i) 30 min; (j−l) 4 h

The P texture is less common in 2000 series Al alloys. To observe the growth of P- and Goss-oriented grains, RT-39 alloy was annealed at 350 °C for 15−20 min, as shown in Fig. 10. P nuclei derive from grain boundaries, fine bands and Copper grains, and grow by consuming deformed Copper grains (Figs. 10(a, b)). The ODF sections for 15 min show strong Copper + weak (Goss, Brass, and P) textures (Fig. 10(e)). P grains grow from Copper grain 2, Grain 4 (mixed Brass + Goss) transitions into Goss grain 11, as annealing time increases. The misorientation between P grain 5 and Copper grain 1 is 36.24° (Fig. 10(c)), and between P grain 9 and Copper grain 2 is 39.54° (Fig. 10(d)). The {111} pole figure confirms a 32.4−42.9° ⟨111⟩ boundary relationship between P and Copper grains, corresponding to the near 40° ⟨111⟩ tilt boundary (∑7). Deformed Copper grains, consisting of many Copper subgrains, present a dispersed range in the {111} pole figure (Fig. 10(f)).

Figure 11 shows the TEM images of the rolling samples. Increasing the rolling temperature reduces dislocation density but promotes dynamic recrystallization (DRX). The RT-39 and RT-42 alloys contain few DRX grains (Figs. 11(a, b)). Figure 6 indicates that elevated rolling temperatures also encourage the precipitation of S-dispersoids, enhancing dynamic recrystallization and precipitation.

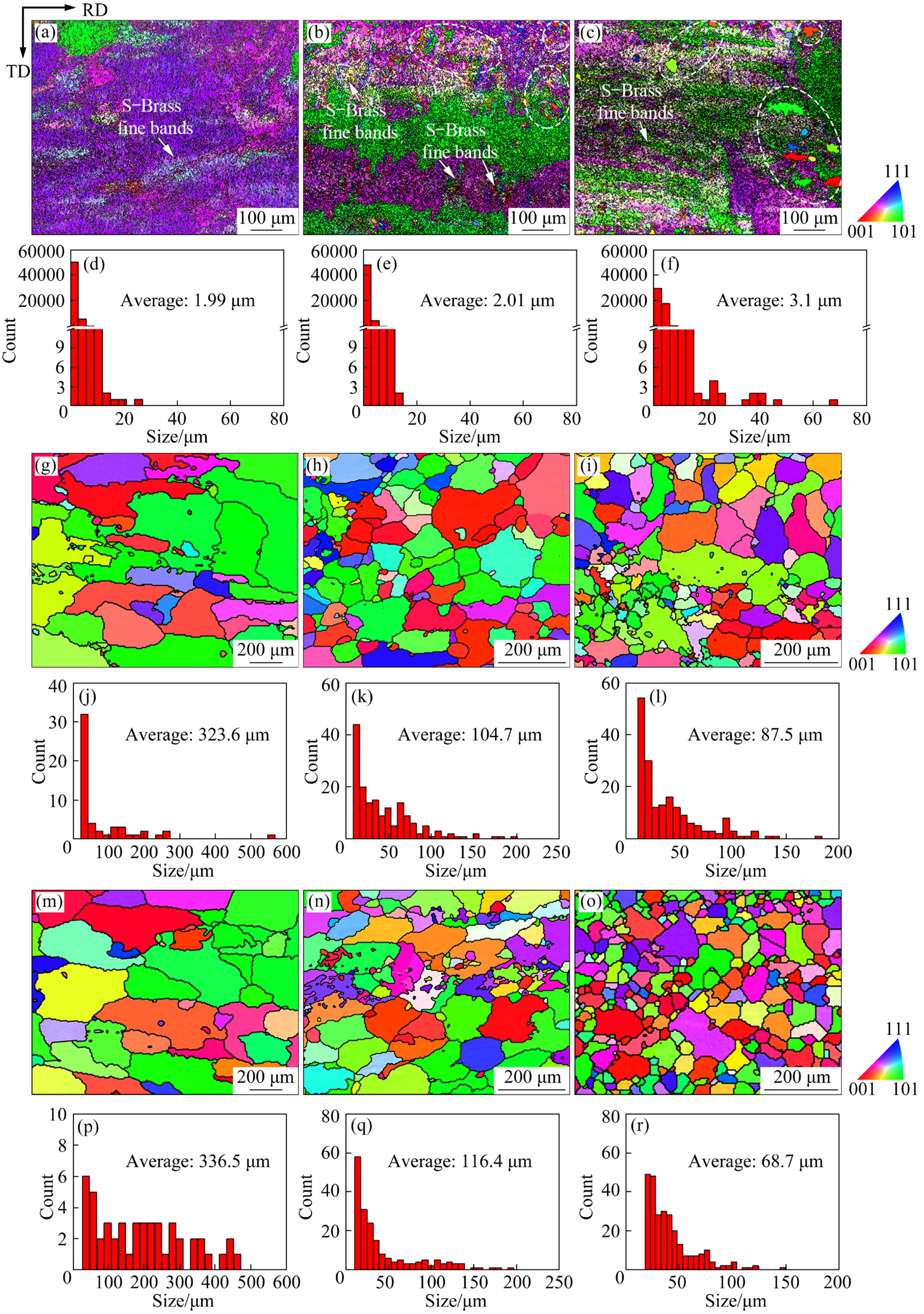

Fig. 7 EBSD results showing microstructure of rolling samples after annealing at 350 °C for 10 min (a−f), 30 min (g−l), and 4 h (m−r); Inverse pole figures of RT-39 alloy (a, g, m), RT-42 alloy (b, h, n) and RT-45 alloy (c, i, o); Grain size distributions of RT-39 alloy (d, j, p), RT-42 alloy (e, k, q) and RT-45 alloy (f, l, r)

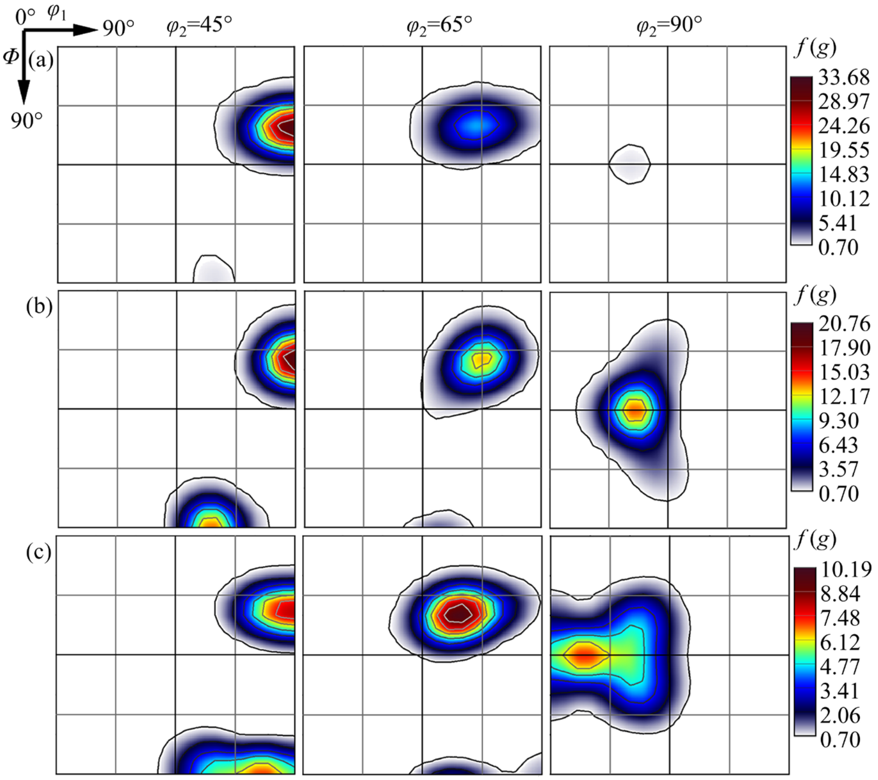

Fig. 8 φ_2=45°, 65°, 90° sections of ODF calculated from EBSD data in Figs. 7(a−c): (a) RT-39 alloy; (b) RT-42 alloy; (c) RT-45 alloy

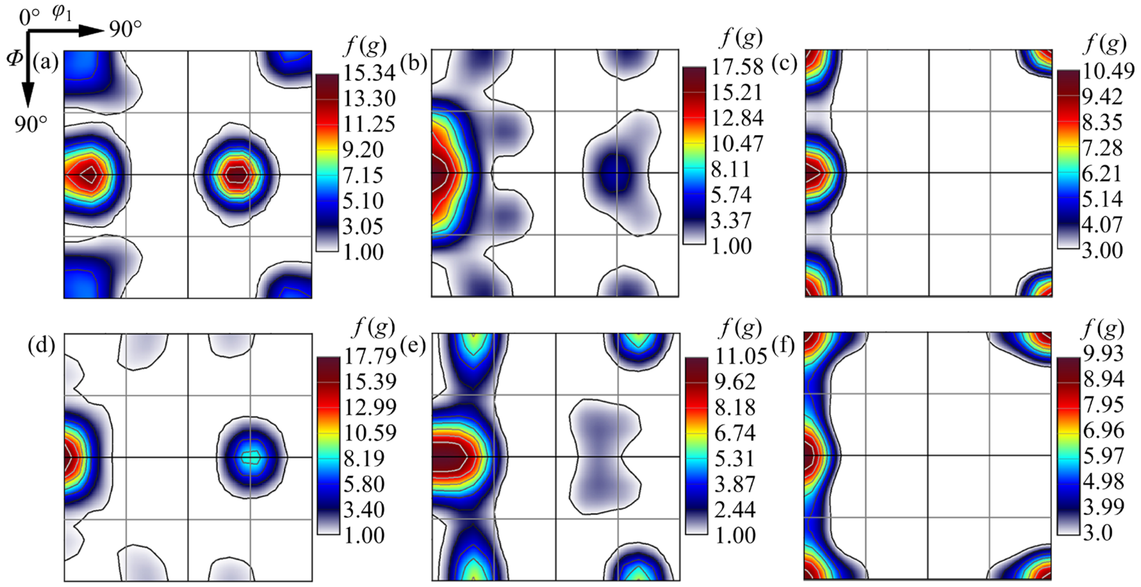

Fig. 9 φ_2=90° sections of ODF calculated from EBSD data in Figs. 7(g−i) and (m−o): (a−c) 30 min; (d−f) 4 h; (a, d) RT-39 alloy; (b, e) RT-42 alloy; (c, f) RT-45 alloy

The RT-45 alloy, has many DRX grains, which especially form near particles (Figs. 11(c, d)). Figure 11(d) is taken from a sample rolled at 480 °C [30].

3.3 Mechanical properties

Figures 12(a−c) display stress−strain curves of the rolling samples after annealing at 350 °C for 5 min to 8 h, with all tests conducted at α= 0°. The mechanical properties show four stages: fast softening (Stage I), rapid strengthening (Stage II), slow strengthening (Stage III), and slow softening (Stage IV) (Figs. 12(d−f)). Initially, all alloys experience softening in the first 0−10 min (0−5 min

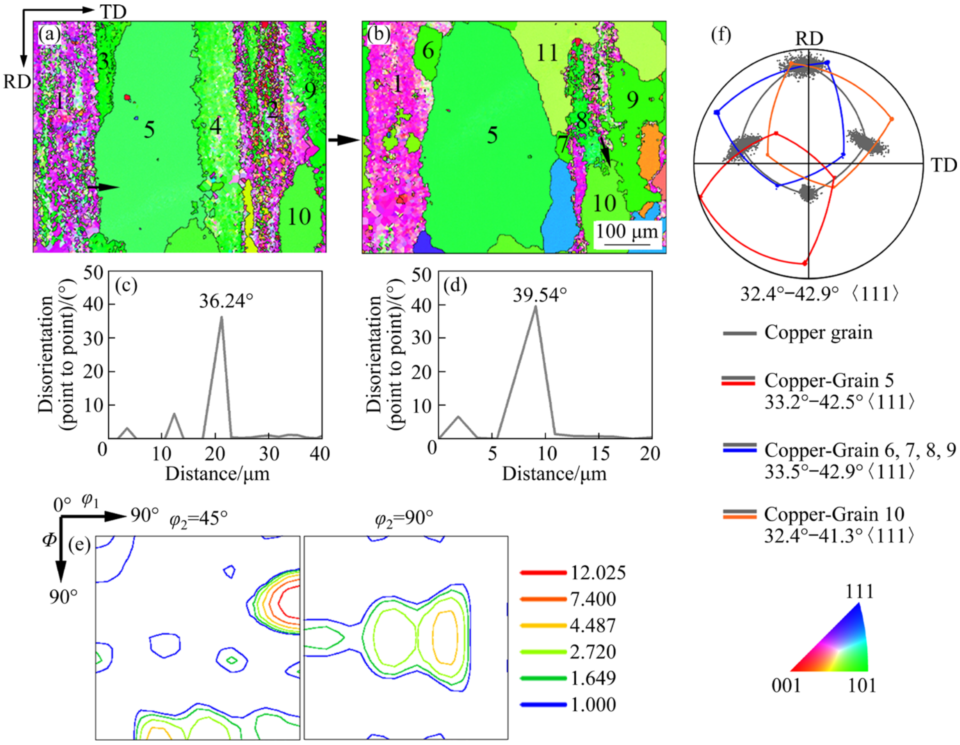

Fig. 10 Quasi-in situ EBSD used to observe formation of Goss and P orientations during annealing at 350 °C, taken from RT-39 alloy: (a) 15 min; (b) 20 min; (c, d) Disorientation angles between Copper and P from black arrows indicated in (a) and (b), respectively; (e) φ_2=45°, 90° sections of ODF calculated from (a); (f) {111} pole figure showing boundary relationship between Copper and P-grains/nuclei (The gray dots with connected lines represent Copper grains)

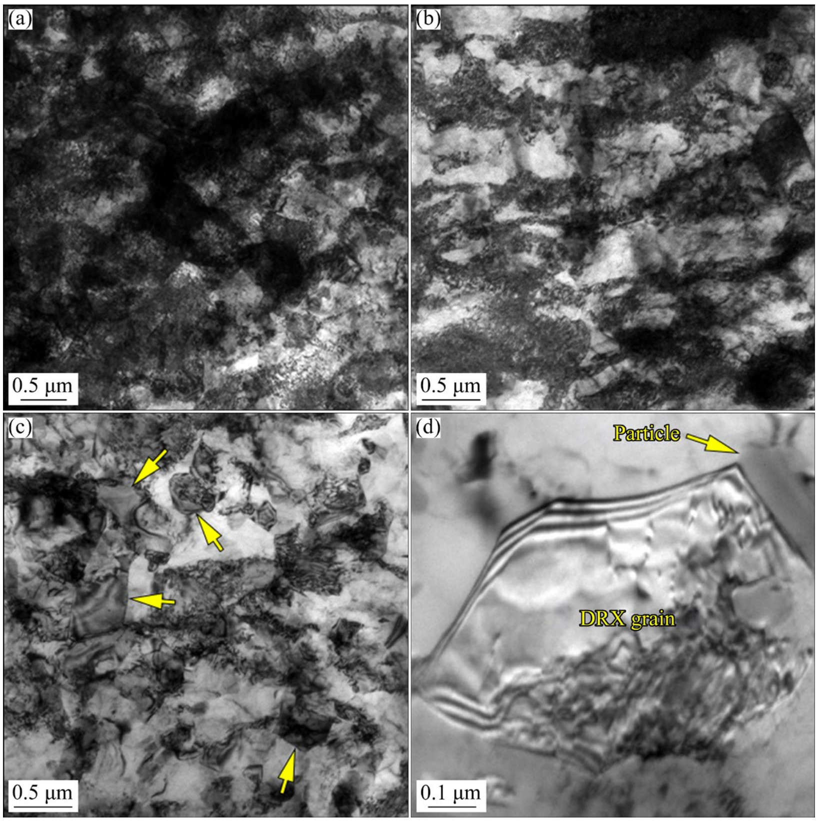

Fig. 11 TEM micrographs showing as-rolled microstructure of alloys: (a) RT-39 alloy; (b) RT-42 alloy; (c) RT-45 alloy (DRX grains are indicated by yellow arrows); (d) High-magnification image showing DRX grain formed near rod-like particle [30]

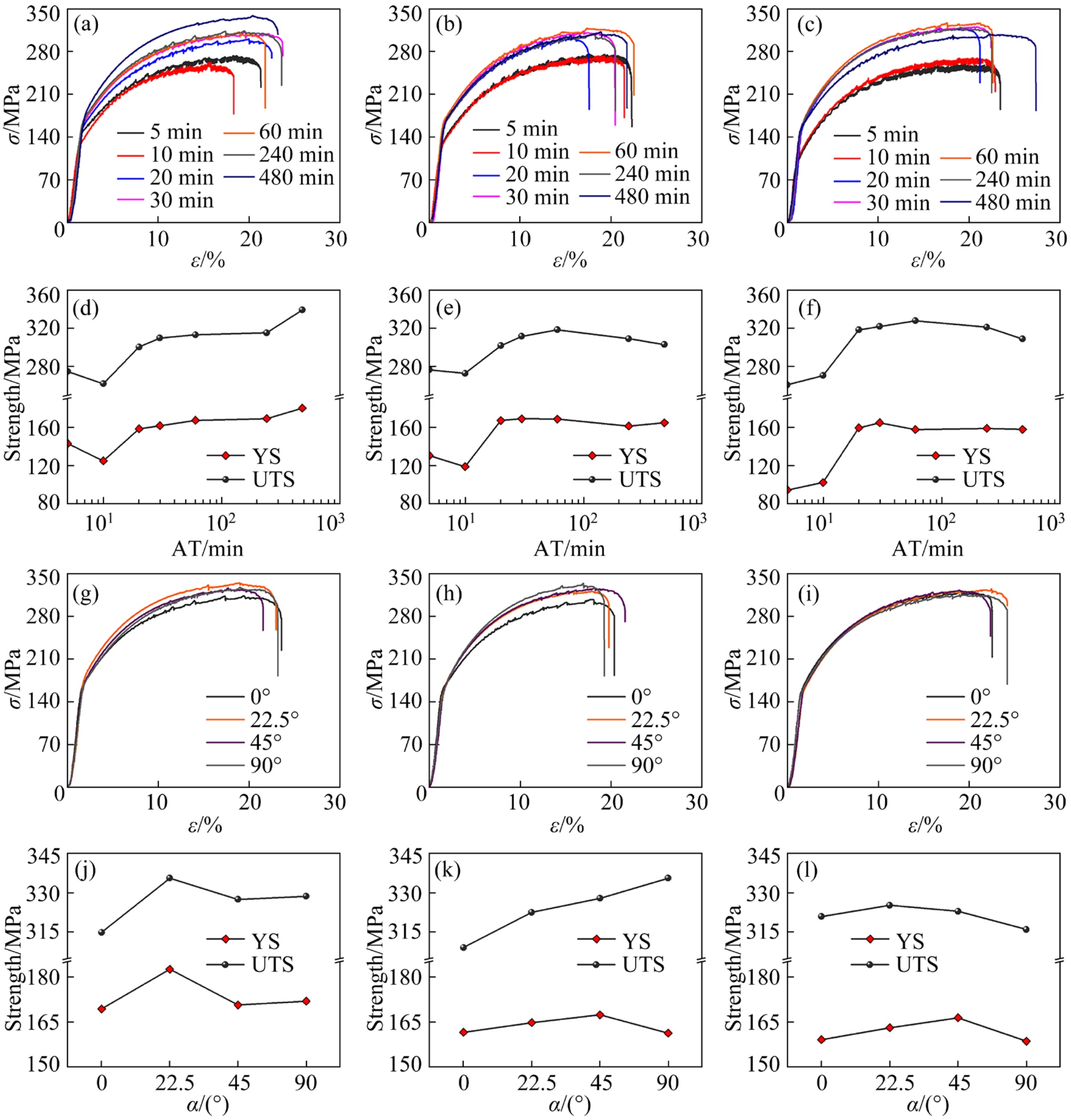

Fig. 12 Tensile property and anisotropy for rolling samples after annealing at 350 °C: (a, d, g, j) RT-39 alloy; (b, e, h, k) RT-42 alloy; (c, f, i, l) RT-45 alloy; (a−c) Stress−strain curves with increasing annealing time from 5 min to 8 h; (d−f) YS and UTS evolution with annealing time (AT); (g−i) Stress−strain curves at different *α* angles of 0°, 22.5°, 45° and 90° for rolling samples after annealing at 350 °C for 4 h; (j−l) YS and UTS evolution with *α*

for the RT-45 alloy). Yield strength (YS) and ultimate tensile strength (UTS) increase quickly between 10 and 20 min. In RT-39 alloy, YS and UTS steadily rise from 20 min to 8 h, reaching 180.4 and 339.3 MPa, respectively, the highest among all the alloys. RT-42 and RT-45 alloys show maximum YS at 30 min (169.2 and 161.1 MPa), with UTS peak at 60 min. After the peaks, both alloys experience slow softening, leading to a significant decrease in UTS and a slight drop in YS (Figs. 12(e, f)). After 8 h of annealing at 350 °C, RT-45 alloy shows a notable increase in elongation (Fig. 12(c)). The observed strengthening and softening behaviors likely correlate with the development of recrystallized textures and grain structures. Figure 13 illustrates the YS/UTS ratio over the annealing time (AT), with RT-45 alloy exhibiting the lowest ratio.

Figures 12(g−i) show the stress−strain curves at different *α* angles of 0°, 22.5°, 45° and 90° for the rolling samples annealed at 350 °C for 4 h. The results demonstrate more pronounced plastic anisotropy in the RT-39 and RT-42 alloys compared with RT-45 alloy. In the RT-39 alloy, UTS increases from 314.9 MPa at *α*=0° to 328.7 MPa at *α*=22.5°

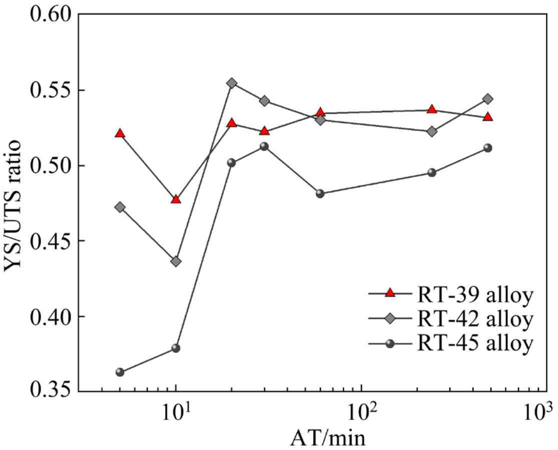

Fig. 13 Evolution of YS/UTS ratio with increasing annealing time

(Fig. 12(j)). The RT-42 alloy has a minimum UTS of 309.1 MPa at α=0° and a maximum of 335.5 MPa at α=90° (Fig. 12(k)). RT-45 alloy shows the highest YS (166.5 MPa) at α= 45°, with UTS showing only minor variations (Fig. 12(l))

Figure 14 shows the through-thickness microhardness profiles of the rolling samples after annealing at 350 °C for 10 min, 30 min, and 4 h. The microhardness gradually increases from the surface to the center for all alloys, indicating that the near-center layer is harder than the surface layer. The annealing time of 10 min results in lower microhardness compared to 30 min and 4 h. Despite minor fluctuations, the hardening behavior in the RT-39 alloy is more prominent than that in the RT-42 and RT-45 alloys. The surface of the annealed plate consists of random texture components and fine equiaxed grains, while the center layers are dominated by strong Goss, P or Cube texture. This results in higher microhardness from the surface to the center. The RT-39 alloy, with a strong P texture, exhibits the highest hardening response among the three alloys.

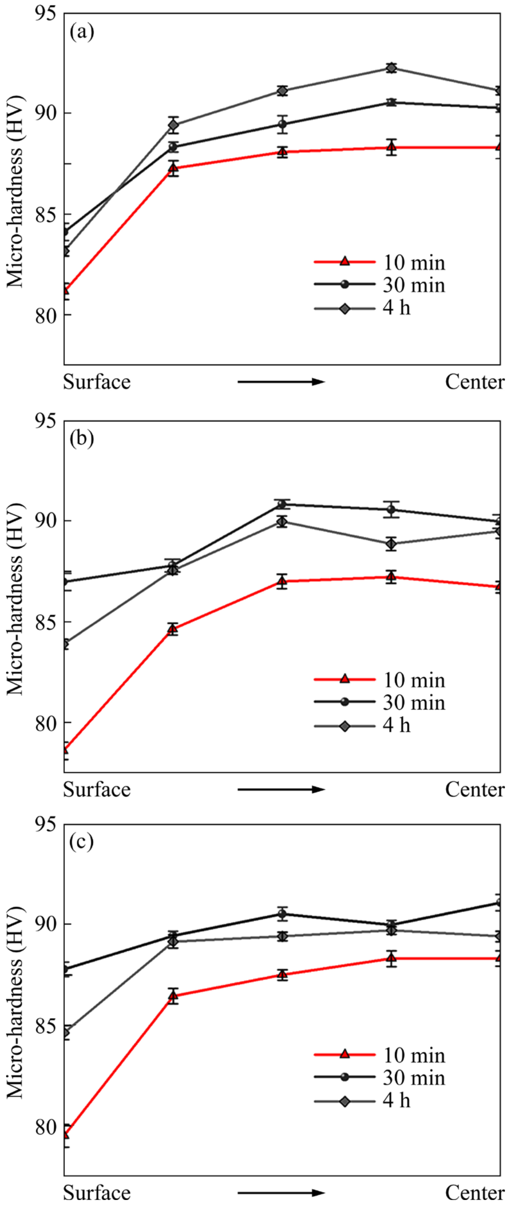

Fig. 14 Through-thickness microhardness profiles of rolling samples after annealing at 350 °C for 10 min, 30 min and 4 h: (a) RT-39 alloy; (b) RT-42 alloy; (c) RT-45 alloy

4 Discussion

4.1 Texture development and grain refining

Increasing the rolling temperature results in a reduction of the $f(g)_{\max(\text{Copper})}/f(g)_{\max(\text{Brass})}$ ratio. This can be attributed to two key factors. (1) Fewer S−Brass fine bands are formed in the RT-39 alloy. However, when the rolling temperature increases from 390 to 450 °C, dynamic recrystallization is promoted, accelerating the formation of S−Brass fine bands and resulting in a texture transition from Copper to S and finally to Brass. (2) The activation of non-octahedral slip systems including $\{110\}\langle 110\rangle$ and $\{100\}\langle 110\rangle$ produces strong Copper and S components, respectively [26]. As the rolling temperature increases, the $\{111\}\langle 110\rangle$ and/or $\{112\}\langle 110\rangle$ slip system becomes dominant, leading to the enhancement of Brass texture [28,29,37]. Furthermore, the studied Al−Cu−Mg alloy has a higher Cu/Mg mass ratio than the typical 2524 alloy, leading to a higher SFE [27], which further promotes the formation of a strong Copper texture.

As discussed, rolling temperature has a significant effect on both the rolling texture and microstructure, which in turn influence the recrystallization texture and grain structure. The relationship between the Copper/Brass ratio (x) and the P/Goss ratio (y) can be described by $\varphi_{\mathrm{P}}/\varphi_{\mathrm{Goss}}=-0.3731+1.08667\varphi_{\mathrm{Copper}}/\varphi_{\mathrm{Brass}}$ for volume fraction (φ) and $f(g)_{\max(\mathrm{P})}/f(g)_{\max(\mathrm{Goss})}=-0.65926+1.27549f(g)_{\max(\mathrm{Copper})}/f(g)_{\max(\mathrm{Brass})}$ for $f(g)$. This relationship suggests that for a strong presence of P texture, the $f(g)_{\max(\mathrm{Copper})}/f(g)_{\max(\mathrm{Brass})}$ needs to be greater than 0.7 in the alloy. ZHAO et al [21] noted that Goss texture typically derives from Brass deformed grains, supporting the $\sum 9$ (i.e., 35°⟨110⟩) boundary migration mechanism. Figure 10 demonstrates that P-oriented grains can originate from grain boundaries, fine bands, and deformed Copper grains, with their growth being closely linked to the preferential grain boundary relationship near 40°⟨111⟩, which exhibits the highest migration rate of all boundaries [22,25,38].

Deformed Brass and S parent grains act as the growth sources of recrystallized Cube [21,22]. The S texture in RT-39 and RT-42 alloys is stronger and has a higher volume fraction than in RT-45 alloy, whereas the Cube texture in RT-39 and RT-42 alloys is relatively weak after annealing. This suggests that the Cube texture is likely independent of the deformed S texture, influenced instead by factors such as the density of S-dispersoids and increased S−Brass fine bands. In RT-39 alloy, the low occurrence of S-dispersoids reduces dynamic recrystallization and the formation of S−Brass fine bands, inhibiting texture transformation along the β-fiber. In contrast, elevated rolling temperatures promote S-dispersoid precipitation, enhancing dynamic recrystallization and increasing S−Brass fine bands in RT-42 and RT-45 alloys. These factors result in the fastest recrystallization rate in RT-45 alloy, which is responsible for the strong presence of Cube texture [13]. Grain refinement can be summarized as: (1) Subgrain boundary migration is pinned by S-dispersoids during annealing, more so in high-temperature rolled plates; (2) The increasing number of S−Brass fine bands offers additional nucleation sites, which hinder boundary migration; (3) Higher rolling temperatures reduce the number of P nuclei during annealing, thus decreasing the preferred 40°⟨111⟩ tilt grain boundaries, inhibiting grain growth. These factors lead to finer recrystallized grains at higher rolling temperatures.

4.2 Texture strengthening and softening

During annealing at 350 °C, the solubility or precipitation of θ-, S-, and T-particles is difficult. Figure 12 shows that the tensile strength response to annealing time involves four stages. High-density dislocations recover early in annealing, around 10 min, leading to Stage I. Combined with Figs. 6, 7, and 12, the transition from Stages I to II depends on the formation of strong Goss, P, and Cube textures.

According to the Hall−Petch equation $\Delta\sigma_{\mathrm{GB}}=kd^{-1/2}$ [39], where $k\approx0.1\ \mathrm{MPa\cdot m^{1/2}}$ for Al [40], the grain size contribution (Figs. 7(p−r)) to yield stress is estimated to be 5.5, 9.3 and 12.1 MPa in RT-39, RT-42, and RT-45 alloys, respectively. Despite RT-39 and RT-42 alloys having larger grains, higher yield stress is observed at α=0° (Figs. 7 and 12), contradicting the Hall−Petch relationship. Figures 15(a−c) show the Schmid factors for Goss, P, and Cube orientations, revealing that P has a lower Schmid factor than Goss and Cube at α=0°. Moreover, Cube has a higher Schmid factor than Goss. The P texture is categorized as a “hard orientation,” while Goss and Cube are “soft orientations.” Based on the Schmid’s law, dislocations should encounter lower slip resistance in Goss- and Cube-grains, with higher Schmid factor than in P-grains. Consequently, RT-39 and RT-42 alloys, which contain P texture, show higher yield strengths than RT-45 alloy.

Furthermore, longer annealing time weakens Goss and P but enhances Cube due to lattice rotation, with Goss rotating toward Cube. Prolonged annealing time improves yield and flow stress in RT-39 alloy, while RT-42 and RT-45 alloys soften (Stage IV). Among the three orientations, the {111} slip plane of Cube is the closest to the maximum CRSS direction. As Cube texture intensity increases, the {111} slip planes of Cube grains move closer to 45° from the RD direction, reducing the CRSS required for dislocation slip. Thus, enhanced Cube contributes to softening.

4.3 Effect of texture and grain structure on anisotropy

As shown in Figs. 15(a−c), the Schmid factor of Goss-, P-, and Cube-grains decreases as α increases from 0° to 45°. Goss- and P-grains exhibit the highest Schmid factors at α=90°, while the Schmid factor for

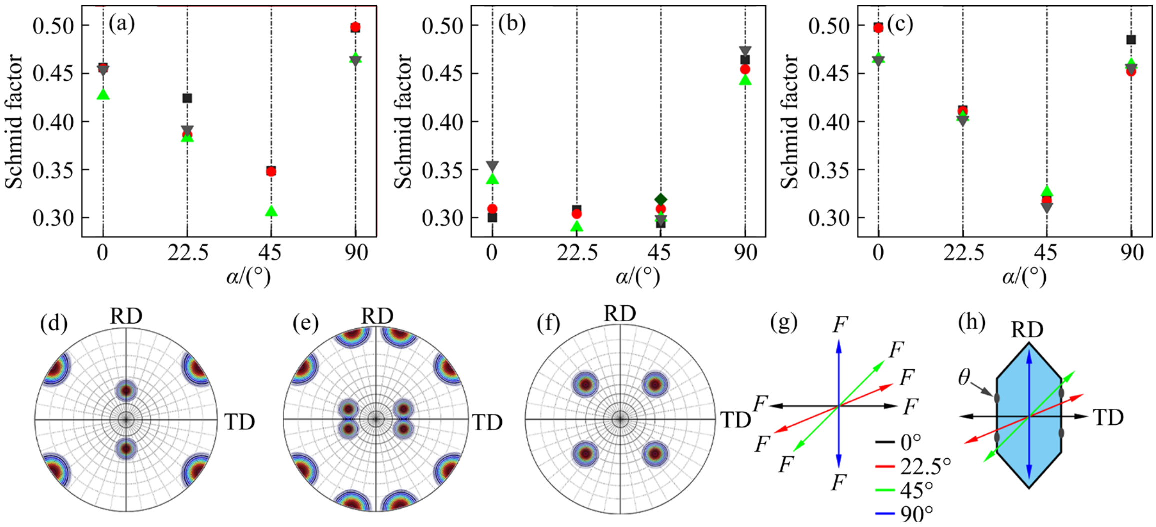

Fig. 15 (a−c) Schmid factor of Goss-, P- and Cube-oriented grains calculated from different α angles from Fig. 7(g), respectively; (d−f) {111} pole figures for standard Goss, P and Cube textures, respectively; (g) Loading force (F) direction; (h) Correlation between loading force direction and microstructure

Cube-grains remains the same at α=0° and 90°. The lowest Schmid factor occurs at α=45°. Figures 15(d−g) show the relationships between the α angles and the {111} slip planes of Goss-, Cube-, and P-grains. At α=0°, the {111} slip planes of Goss and Cube align with the CRSS direction, promoting dislocation slip. At α=45°, the loading direction is parallel to the {111} slip planes of Goss and Cube, which minimizes the Schmid factor and suppresses dislocation slip, correlating with the highest yield stress in Goss- and Goss + Cube-controlled RT-42 and RT-45 alloys. For P-grains, most {111} slip planes align with the TD at 22.5° and 35°. In RT-39 alloy with strong P-texture, the maximum yield stress occurs at α=22.5° due to the lower Schmid factor of P-grains at this angle.

In addition, anisotropy is also influenced by grain structure and θ-particles at boundaries. Figure 15(h) presents a diagram showing the correlation between loading force and microstructural features. The worst tensile properties occur at α=0° (Fig. 12), which is due to multiple factors. First, θ-particles along grain boundaries, where the loading stress is nearly perpendicular to these boundaries at α=0°, have weaker binding forces at the interface compared to other cases, promoting crack nucleation. Second, the alignment of the {111} slip planes with the CRSS direction reduces dislocation slip resistance. In summary, plates with strong (Goss and P) + weak Cube textures and elongated grain structures exhibit more pronounced anisotropy than those with strong Goss + Cube textures and fine equiaxed grains. Elevated rolling temperatures help refine Goss- and Cube-grains and reduce the anisotropy in as-annealed alloys.

5 Conclusions

(1) Elevated rolling temperature reduces the $f(g)_{\max(\text{Copper})}/f(g)_{\max(\text{Brass})}$ ratio, increases S−Brass fine bands, and promotes the precipitation of S-dispersoids. These factors result in finer recrystallized grain sizes at higher rolling temperatures. After annealing at 350 °C, the dominant recrystallization textures transition from Goss + P to Goss, and then to Goss + Cube as the rolling temperature increases.

(2) During annealing at 350 °C, tensile strength undergoes four stages: fast softening (I), rapid strengthening (II), slow strengthening (III), and slow softening (IV). The transition from Stages I to II is driven by the formation of strong Goss, P and Cube textures, while Stage IV is associated with enhanced Cube texture. The P-grains, with their lower-Schmid factor, contribute more to yield strength than Goss- and Cube-grains.

(3) Plates with strong (Goss and P) + weak Cube textures and a heavily elongated grain structure along the RD direction, or those with strong Goss + weak (P and Cube) and moderate grain size, exhibit higher anisotropy compared to those with dominant Goss + Cube textures and finer equiaxed grains,

which show the lowest YS/UTS ratio and minimal anisotropy.

CRediT authorship contribution statement

Guang-yu HE: Methodology, Investigation, Writing − Original draft, Review & editing; **Zhi-yi LIU:** Conceptualization, Methodology, Validation, Formal analysis, Investigation, Resources, Writing − Review & editing; **Yang-cheng HU:** Methodology, Formal analysis, Writing − Review & editing; **Qian JIANG:** Formal analysis, Writing − Review & editing; **M. S. QURASHI:** Formal analysis, Writing − Review & editing.

Declaration of competing interest

The authors declare that they have no known competing financial interests or personal relationships that could have appeared to influence the work reported in this paper.

Acknowledgments

The authors are grateful for financial support from the National Key Research and Development Program of China (No. 2016YFB0300900), the National Key Fundamental Research Project of China (No. 2012CB619506−3), and the National Natural Science Foundation of China (No. 51171209).

References

[1] BRAY G H, GLAZOV M, RIOJA R J, LI D, GANGLOFF R P. Effect of artificial aging on the fatigue crack propagation resistance of 2000 series aluminum alloys [J]. International Journal of Fatigue, 2001, 23: 265−276.

[2] DURSUN T, SOUTIS C. Recent developments in advanced aircraft aluminium alloys [J]. Materials & Design, 2014, 56: 862−871.

[3] ZHANG Xue-song, CHEN Yong-jun, HU Jun-ling. Recent advances in the development of aerospace materials [J]. Progress in Aerospace Sciences, 2018, 97(2): 22−34.

[4] MASUDA T, SAUVAGE X, HIROSAWA S, HORITA Z. Achieving highly strengthened Al−Cu−Mg alloy by grain refinement and grain boundary segregation [J]. Materials Science and Engineering: A, 2020, 793(8): 139668.

[5] KHAN I N, STARINK M J, YAN J L. A model for precipitation kinetics and strengthening in Al−Cu−Mg alloys [J]. Materials Science and Engineering: A, 2008, 472(1/2): 66−74.

[6] SUN Wen-wen, ZHU Yu-man, MARCEAU R, WANG Ling-yu, ZHANG Qi, GAO Xiang, HUTCHINSON C. Precipitation strengthening of aluminum alloys by room-temperature cyclic plasticity [J]. Science, 2019, 363 (6430): 972−975.

[7] FAN Cai-he, LI Yi-hui, WU Qin, OU Ling, HU Ze-yi, NI Yu-meng, YANG Jian-jun. Effect of cold rolling deformation on microstructure evolution and mechanical properties of spray formed Al−Zn−Mg−Cu−Cr alloys [J]. Transactions of Nonferrous Metals Society of China, 2024, 34(8): 2442−2454.

[8] YANG Xian-wen, YE Ling-ying, ZHANG Yong, CHENG Quan-shi. Effect of interrupted aging on mechanical properties and corrosion resistance of 7A75 aluminum alloy [J]. Transactions of Nonferrous Metals Society of China, 2024, 34: 2415−2430.

[9] ENGLER O, AEGERTER J. Texture and anisotropy in the Al−Mg alloy AA 5005−Part II: Correlation of texture and anisotropic properties [J]. Materials Science and Engineering: A, 2014, 618 (11): 663−671.

[10] KUMAR D, SHANKAR G, PRASHANTH K G, SUWAS S. Texture dependent strain hardening in additively manufactured stainless steel 316L [J]. Materials Science and Engineering: A, 2021, 820(7): 141483.

[11] LU Ding-ding, LIN Ben, LIU Tian-le, DENG San-xi, GUO You-jie, LI Jin-feng, LIU Dan-yang. Effect of grain structure on fatigue crack propagation behavior of Al−Cu−Li alloys [J]. Journal of Materials Science & Technology, 2023, 148(6): 75−89.

[12] KAZEMI-NAVAEE A, JAMAATI R, JAMSHIDI AVAL H. Effect of single roll drive rolling on microstructure, texture, and mechanical property anisotropy of Al−5.6Zn−2.5Mg−1.4Cu aluminum alloy [J]. Transactions of Nonferrous Metals Society of China, 2023, 33(11): 3266−3281.

[13] HUANG K, MARTHINSEN K. The effect of heating rate on the softening behaviour of a deformed Al−Mn alloy with strong and weak concurrent precipitation [J]. Materials Characterization, 2015, 110(12): 215−221.

[14] FANG Hong-jie, LIU Hui, YAN Yang, LUO Xi-er, XU Xiang-chun, CHU Xin, LU Yu-jiao, YU Kun, WANG Dian-gang. Evolution of texture, microstructure, tensile strength and corrosion properties of annealed Al−Mg−Sc−Zr alloys [J]. Materials Science and Engineering: A, 2021, 804 (2): 140682.

[15] LIU Fei, LIU Zhi-yi, HE Guang-yu, OU Lin-nan. Dislocation ordering and texture strengthening of naturally aged Al−Cu−Mg alloy [J]. Journal of Materials Science and Technology, 2022, 118(8): 1−14.

[16] CHEN Y Q, PAN S P, ZHOU M Z, YI D Q, XU D Z, XU Y F. Effects of inclusions, grain boundaries and grain orientations on the fatigue crack initiation and propagation behavior of 2524-T3 Al alloy [J]. Materials Science and Engineering: A, 2013, 580(9): 150−158.

[17] WEI Li-li, PAN Qing-lin, HUANG Hong-feng, FENG Lei, WANG Yi-lin. Influence of grain structure and crystallographic orientation on fatigue crack propagation behavior of 7050 alloy thick plate [J]. International Journal of Fatigue, 2014, 66(9): 55−64.

[18] LIU Zhi-yi, LI Fu-dong, XIA Peng, BAI Song, GU Yan-xia, YU Di-er, ZENG Su-min. Mechanisms for Goss-grains induced crack deflection and enhanced fatigue crack propagation resistance in fatigue stage II of an AA2524 alloy [J]. Materials Science and Engineering: A, 2015, 625(2): 271−277.

[19] LI Fu-dong, LIU Zhi-yi, WU Wen-ting, XIA Peng, YING Pu-you, ZHOU Ya-ru, LIU Wen-juan, LU Lu-qing, WANG An. Enhanced fatigue crack propagation resistance of Al−Cu−Mg alloy by intensifying Goss texture and refining Goss grains [J]. Materials Science and Engineering: A, 2017, 679(1): 204−214.

[20] HU Yang-cheng, LIU Zhi-yi, ZHAO Qi, BAI Song, LIU Fei. P-texture effect on the fatigue crack propagation resistance in an Al−Cu−Mg alloy bearing a small amount of silver [J]. Materials, 2018, 11(12): 2481.

[21] ZHAO Qi, LIU Zhi-yi, BAI Song, LI Sha-sha, HU Yang-cheng, XIA Peng. Coincidence site lattice boundary mechanism for the preferred growth of Goss and Cube grains

during annealing in an Al−Cu−Mg alloy [J]. Materials Characterization, 2018, 141(7): 193−211.

[22] MAO Wei-min, YANG Ping. Formation mechanisms of recrystallization textures in aluminum sheets based on theories of oriented nucleation and oriented growth [J]. Transactions of Nonferrous Metals Society of China, 2014, 24(6): 1635−1644.

[23] MA M, WANG W X, ZHANG J X, LIU W C. The role of oriented growth in P texture development in Al−Mn−Mg aluminum alloy [J]. Journal of Materials Engineering and Performance, 2014, 23(9): 3257−3265.

[24] HUANG K, LI Y J, MARTHINSEN K. Factors affecting the strength of P {011}⟨566⟩-texture after annealing of a cold-rolled Al−Mn−Fe−Si alloy [J]. Journal of Materials Science, 2015, 50(14): 5091−5103.

[25] HUANG K, ZHANG K, MARTHINSEN K, LOGÉ R E. Controlling grain structure and texture in Al−Mn from the competition between precipitation and recrystallization [J]. Acta Materialia, 2017, 141: 360−373.

[26] BACROIX B, JONAS J J. The influence of non-octahedral slip on texture development in FCC metals [J]. Textures Stress and Microstructure, 1988, 8: 267−311.

[27] SCHULTHESS T C, TURCHI P E A, GONIS A, NIEH T G. Systematic study of stacking fault energies of random Al-based alloys [J]. Acta Materialia, 1998, 46(6): 2215−2221.

[28] CONTREPOIS Q, MAURICE C, DRIVER J H. Hot rolling textures of Al−Cu−Li and Al−Zn−Mg−Cu aeronautical alloys: Experiments and simulations to high strains [J]. Materials Science and Engineering A, 2010, 527(27/28): 7305−7312.

[29] XIA Peng, LIU Zhi-yi, WU Wen-ting, ZHAO Qi, LU Lu-qing, BAI Song. Texture evolution in an Al−Cu−Mg alloy during hot rolling [J]. Journal of Materials Engineering and Performance, 2018, 27(7): 3255−3267.

[30] HE Guang-yu, LIU Zhi-yi, LIU Fei. Effects of dislocation slip behaviour and second-phase particles on hot rolled texture of an Al−Cu−Mg alloy with a high Cu/Mg ratio [J]. Journal of Alloys and Compounds, 2022, 911(8): 165085.

[31] BUNGE H J. Texture analysis in materials science [M]. London: Butterworths, 1982.

[32] TANG Jian-Guo, ZHANG Xin-Ming, DENG Yun-Lai, DU Yu-Xuan, CHEN Zhi-Yong. Texture decomposition with particle swarm optimization method [J]. Computational Materials Science, 2006, 38(2): 395−399.

[33] BEAUSIR B, FUNDENBERGER J J. Analysis tools for electron and X-ray diffraction. ATEX-software [Z]. www.atex-software.eu, Université de Lorraine-Metz, 2017.

[34] HIGUERA-COBOS O F, CABRERA J M. Mechanical, microstructural and electrical evolution of commercially pure copper processed by equal channel angular extrusion [J]. Materials Science and Engineering A, 2013, 571(6): 103−114.

[35] LUGO N, LLORCA N, SUÑOL J J, CABRERA J M. Thermal stability of ultrafine grains size of pure copper obtained by equal-channel angular pressing [J]. Journal of Materials Science, 2010, 45: 2264−2273.

[36] ZHAO Qi, LIU Zhi-yi, LI Sha-sha, HU Yang-cheng, BAI Song. Effect of S phase characteristics on the formation of recrystallization textures of an Al−Cu−Mg alloy [J]. Journal of Alloys and Compounds, 2018, 747(5): 293−305.

[37] ZHAO Qi, LIU Zhi-yi, LI Sha-sha, HUANG Tian-tian, XIA Peng, LU Lu-qing. Evolution of the Brass texture in an Al−Cu−Mg alloy during hot rolling [J]. Journal of Alloys and Compounds, 2017, 691: 786−799.

[38] FAN G H, ZHANG Y B, DRIVER J H, JENSEN D J. Oriented growth during recrystallization revisited in three dimensions [J]. Scripta Materialia, 2014, 72−73(2): 9−12.

[39] CHEN Z G, REN J K, YUAN Z G, RINGER S P. Enhanced strength-plasticity combination in an Al−Cu−Mg alloy: Atomic scale microstructure regulation and strengthening mechanisms [J]. Materials Science and Engineering: A, 2020, 787: 139447.

[40] EMBURY J D. Strengthening mechanisms in Al alloys-An overview of natural limits and engineering possibilities [J]. Materials Science Forum, 1996, 217/218/219/220/221/222: 57−70.

织构和晶粒结构对退火态高 Cu/Mg 质量比 Al−Cu−Mg 合金拉伸强度和各向异性的影响

何光宇 [1,2]，刘志义 [1,2]，胡扬城 [1,2]，蒋 倩 [1,2]，M. S. QURASHI [1,2]

1. 中南大学 材料科学与工程学院，长沙 410083；
2. 中南大学 有色金属材料科学与工程教育部重点实验室，长沙 410083

摘 要：借助 XRD、DSC、SEM、EBSD 和 TEM 研究退火过程中织构和晶粒结构的演变及其对拉伸强度和各向异性的影响。结果表明，升高热轧温度降低$f(g)_{\max(\mathrm{Copper})}/f(g)_{\max(\mathrm{Brass})}$比，增加 S−Brass 微取向带，促进 S 弥散相的析出，造成更细的再结晶晶粒。随着热轧温度的升高，控制的再结晶织构逐渐由 Goss＋P 向 Goss 再向 Goss＋Cube 转变。350 ℃退火下拉伸强度响应分为快速软化阶段I、快速强化阶段II、缓慢强化阶段III和缓慢软化阶段IV 4 个阶段。强 Goss、P 织构的形成驱动阶段I到II的转变，阶段IV与增强的 Cube 织构有关。具有 Goss＋Cube 织构和细等轴晶粒的板材呈现最低的 YS/UTS 比和最小的各向异性。

关键词：Al−Cu−Mg 合金；Goss 织构；P 织构；Cube 织构；晶粒结构；拉伸强度；各向异性

(Edited by Xiang-qun LI)